Nanoscale

Accepted Manuscript

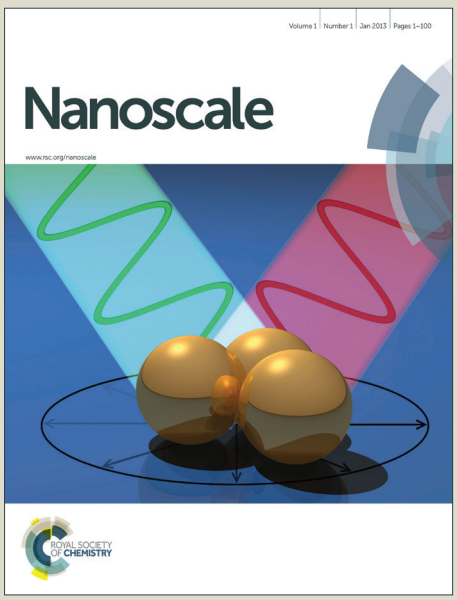

ROYAL SOCIETY OF CHEMISTRY

www.rsc.org/nanoscale

Strontium Eluting Graphene Hybrid Nanoparticles Augment Osteogenesis in 3D Tissue Scaffold

Sachin Kumar and Kaushik Chatterjee*

Department of Materials Engineering

Indian Institute of Science, Bangalore 560012 India

* *author to whom all correspondence should be addressed*

Email: kchatterjee@materials.iisc.ernet.in

Tel: +91-80-22933408

Abstract

The objective of this work was to prepare hybrid nanoparticles of graphene sheets decorated with strontium metallic nanoparticles and demonstrate its advantages in bone tissue engineering. Strontium-decorated reduced graphene oxide (RGO_Sr) hybrid nanoparticles were synthesized by facile reduction of graphene oxide and strontium nitrate. X-ray diffraction, transmission electron microscopy, and atomic force microscopy revealed that the hybrid particles were composed of RGO sheets decorated with 200 – 300 nm metallic strontium particles. Thermal gravimetric analysis further confirmed the composition of the hybrid particles as 22 wt% of strontium. Macroporous tissue scaffolds were prepared incorporating RGO_Sr particles in poly (ε-caprolactone) (PCL). The PCL/RGO_Sr scaffolds were found to elute strontium ions in aqueous medium. Osteoblast proliferation and differentiation was significantly higher in the PCL scaffolds containing the RGO_Sr particles in contrast to neat PCL and PCL/RGO scaffolds. The increased biological activity can be attributed to the release of strontium ions from the hybrid nanoparticles. This study demonstrates that composites prepared using hybrid nanoparticles that elute strontium ions can be used to prepare multifunctional scaffolds with good mechanical and osteoinductive properties. These findings have important implications for designing the next generation of biomaterials for use in tissue regeneration.

Keywords: Graphene; Hybrid nanoparticles; Polymer nanocomposites; Tissue scaffolds; Osteogenesis

1. Introduction

In recent years, graphene has emerged as a promising nanomaterial for a wide variety of biomedical applications such as drug delivery, biosensing, tissue engineering, and imaging.[1-3] In particular, owing to its extraordinary mechanical and electrical properties, graphene-based polymer nanocomposites are being studied for potential use as tissue scaffolds for orthopedic and neural tissue regeneration.[4, 5] For orthopaedic applications, although graphene can significantly increase the mechanical properties of the polymer matrix, it lacks chemical moieties that may stimulate osteogenesis.[6] In contrast, ceramic nanoparticles such as calcium phosphate are typically less effective in strengthening the polymer matrix but have been shown to stimulate osteogenic differentiation of osteoprogentior and stem cells.[7, 8] The local release of calcium ions from these nanoparticles when incorporated in the scaffolds is believed to play an important role in stimulating bone cells.[9] Similarly, studies have also reported that strontium ions can stimulate osteoblasts and down regulate osteoclast activity.[10, 11] Strontium ranelate is a popular drug used to treat osteoporosis.[12, 13] More recently, a number of in vitro and in vivo studies have reported on enhanced osteogenesis with the use of strontium-containing bioceramics.[14, 15] In bone tissue engineering it is important to design a three dimensional (3D) scaffold to provide a micro-environment for the cells. Despite good bone regeneration properties, the brittle nature of strontium substituted bioceramics limits their use for load bearing applications. In addition, the silica and phosphate content in these bioceramics results in large undesired increase in pH due to the initial burst release of these alkali ions upon dissolution.[16] As a result, polymer coated strontium-containing bioactive glass scaffolds have also been proposed but the polymer coating impedes the release of strontium ions in the scaffolds.[17]

Polymer nanocomposites mimic the natural mimic the natural architecture of bone, which contains nanoscale hydroxyapatite embedded in polymeric collagen phase and thus,

are well suited for bone tissue engineering. During preparation of scaffolds using polymeric composites containing metallic/ceramic nanoparticles it is ideal to have ultrafine size particles with high surface to volume ratio well dispersed in the polymer matrix. Fine well-dispersed nanoparticles in the composite improve mechanical properties and facilitate the release of ions from the particles. However, fine nanosized metallic particles possess high surface energy, which leads to uncontrolled agglomeration forming large particles to minimize surface energy.[18] Also, it is widely reported that the bioceramic or metallic nanoparticles tend to aggregate in polymer matrix due to their incompatibility with the polymer resulting in deterioration of both mechanical and biological performance.[19, 20] To minimize agglomeration, surfactants can be used to improve the dispersion of the nanoparticles although at the risk of increased cytotoxicity. Recent studies have shown that graphene oxide (GO) or reduced graphene oxide (RGO) acts as substrate to nucleate and facilitate the attachment of metallic particle on the edges and surface of graphene.[21-23]

Towards engineering a mechanically strong yet osteoinductive tissue scaffold, we hypothesized that a graphene-based hybrid nanoparticle that elutes strontium ions could serve as effective nanofiller in polymer scaffolds. The large surface area of the graphene sheets can be used to deposit fine, non-agglormerated metallic nanoparticles with large specific surface area. These hybrid particles can be dispersed in the polymer minimizing the need for surfactants. Thus, these hybrid nanoparticles can serve two objectives for engineering scaffolds for bone tissue regeneration. Graphene sheets would enhance the mechanical properties of the polymer and facilitate effective dispersion of the strontium nanoparticles for improved bioactivity. Hybrid nanomaterials with wide range of tailored properties for multipurpose applications are increasingly being developed to synergistically leverage the properties of the individual components.[24-26] Over the years graphene sheets decorated with polymer, nanotubes, and metallic nanoparticles have been used to prepare composites or

hybrid materials.[21] Unique and facile techniques for synthesising dispersed metallic particles on GO sheets were developed.[22] Dispersed metallic particles bind chemically or electrostatically on graphene derived sheets thus preventing aggregation or restacking of graphene sheets. As a result these hybrid nanoparticles remarkably enhance the performance of the polymer composites prepared using these hybrids.

Whereas a number of such studies have been reported on graphene sheets decorated with various metallic nanoparticles for use in batteries, capacitors, surface-enhanced Raman scattering, and bio-sensor application,[23, 27-29] the potential advantage of such hybrid particles for biomedical applications remains largely unexplored. The bactericidal property of GO sheet decorated with silver nanoparticles was reported recently.[30, 31] There are no reported studies on the use of such particles in regenerative medicine. Our aim was to demonstrate the unique advantages of strontium-graphene hybrid particles in bone tissue engineering. In this study we present a facile synthesis route to prepare reduced graphene oxide sheets decorated with strontium nanocrystals (RGO_Sr). The RGO_Sr hybrid particles were used in polymer matrices for preparation of 3D macroporous scaffolds for bone tissue engineering. Release of strontium ion is shown to promote osteoblast proliferation and mineralization in the scaffolds.

2. Materials and Methods

2.1. Synthesis of GO, RGO and RGO_Sr

Natural graphite flakes (Superior Company) was used to prepare GO by oxidation as proposed by Hummer.[32] 50 mg of as-synthesied GO was dispered in 100 ml ultrapure water (Sartorius) by bath sonication (S.V Scientific). For synthesis of RGO, 1 ml of hydrazine hydrate, the reducing agent, was added to the GO solution under constant stirring and heated to 60° C for 6 h. For the synthesis of RGO_Sr particles, 0.1 M strontium nitrate solution was added to the dispersed GO solution and further sonicated for 15 min. To this mixture, hydrazine hydrate was added under constant stirring and heated as above. The product was obtained by filtration of the solution, rinsed repeatedly with water and vacuum dried for 2 days.

2.2. Characterization of GO, RGO and strontium decorated RGO nanoparticles

The synthesised GO, RGO, and RGO_Sr particles were characterized by X-ray diffraction (XRD, XPERTPro, PANalytical). XRD pattern was obtained using a Cu Kα radiation source (λ= 1.5406Å, 40 kV and 30 mA) with 2θ range of 5° to 70°. Raman spectra (WITEC Raman spectrometer) for the nanoparticles were recorded using a 514 nm wavelength laser excitation source. Thermal gravimetric analysis (TGA, NETZSCH STA 409) was performed on RGO and RGO_Sr) at a constant heating rate of 20° C/min. X-ray photoelectron spectrometer (XPS, Kratos Analytical instrument) spectra of RGO_Sr nanoparticles were measured using Al monochromatic source (1.486 keV).

RGO_Sr particles were also characterized by transmission electron microscopy (TEM, TecnaiTM G2 F30 S-TWIN), scanning electron microscopy (SEM, FEI ESEM Quanta 200) and atomic force microscopy (AFM, NX-10 Park Systems). RGO_Sr particles were dispersed in chloroform by bath sonication. Dispersed RGO_Sr sheets were drop casted

on a TEM grid for characterization. For SEM, few drops of the dispersed RGO_Sr particles were dried placed on an aluminum stub and sputter-coated with gold. For AFM study dispersed RGO_Sr was drop casted on silica substrate and imaged in tapping mode. Surface water wettability of synthesized RGO and RGO_Sr flakes was measured using a video-based optical contact angle goniometer (OCA 15EC, Dataphysics). The contact angles reported represent mean ± S.D. for at least three independent measurements.

2.3. Preparation of porous scaffold

Macroporous PCL nanocomposite scaffolds were prepared by gas foaming technique using ammonium bicarbonate as the effervescent porogen, as reported previously.[33] The RGO_Sr and RGO nanoparticles were dispersed in chloroform by bath sonication for 30 min. PCL (Sigma, M_n = 80000) was dissolved at 0.1 g/mL. The weight fraction of nanoparticles was varied from 1 to 5 wt% of the polymer as detailed in Table 1. 0.13 g of ammonium bicarbonate salt was added into each well of a flat-bottom 96-well polypropylene plate (Sigma). 45 µl of the polymer solution containing the dispersed nanoparticles was added to each well. The plates were centrifuged at 2000 rpm for 2 min and the solvent was evaporated under vacuum. The plates were immersed in deionized water to induce gas foaming and left in water until no gas bubbles were generated, approximately 1 h. Subsequently, the porous scaffolds were vacuum dried for 24 h.

2.4. Scaffold characterization

The architecture of the scaffold was examined using SEM. The presence of strontium in the porous PCL/RGO_Sr scaffolds was chemically confirmed using energy dispersive X-ray (EDX) spectrum. Water contact angle of neat PCL and the composites was measured on cast film. Porosity of gas foamed scaffolds were measured by liquid displacement method.[34] Porous scaffold was immersed in a graduate measuring cylinder having known volume of ethanol (V1). Scaffold was left in the cylinder for 10 min allowing ethanol to penetrate in the

pores. Then the total volume of ethanol and ethanol-soaked scaffold was recorded (V_2). Soaked scaffold was then removed and left over ethanol volume was measured (V_3). The volume difference ($V_2 - V_3$) represents the skeleton volume of scaffold whereas ($V_1 - V_3$) corresponds to void volume of scaffold. The porosity (ε) of the scaffold was calculated as:

$$\varepsilon(\%) = [(V_1 - V_3) / (V_2 - V_3)] *100$$

Inductively coupled plasma-optical emission spectroscopy (ICP-OES, Thermo-iCAP 6000) was used to quantify the release of strontium ions the PCL/RGO_Sr scaffolds. The scaffolds were incubated at 37° C for 3 days in 1 mL ultrapure water. The solution putatively containing the strontium ions eluted from the scaffolds was diluted 20-fold prior to quantification by ICP-OES. A standard curve was generated from serial dilutions of a solution containing known concentration of strontium ions. The release kinetics of strontium ions eluted from the scaffolds containing the hybrid nanoparticles was further characterized over time. PCL/RGO_Sr_5 scaffolds were placed in 1 mL of ultrapure water in closed vials. The tubes were incubated at 37° C. Water containing eluted strontium ions from the scaffolds was collected every 3 days and replenished with fresh ultrapure water. Strontium ions concentration was determined by ICP-OES as above.

The effect of the hybrid nanoparticles on polymer degradation was characterized using cast thin films (7.5 mg) of neat PCL, PCL/RGO_5 and PCL/RGO_Sr_5 were analysed using immersion method.[35] Samples were immersed in 1 mL of ultrapure water and incubated at 37° C. At days 3, 7 and 10, the samples were vacuum dried and weighed. The weight loss (%) was calculated as:

$$\text{Weight loss } (\%) = [(W_0 - W_t)/W_0] \text{ x}100$$

where W_0 is initial weight of sample before degradation, W_t is the weight of sample at given degradation time point. Three independent samples were used for each measurement. In addition to the films, degradation in PCL/RGO_Sr_5 scaffolds was studied at different time intervals by continuous immersion without change of water. Samples were retrieved at 3, 7, 10 and 15 days, and dried. The surface morphology was examined using SEM. The concentration of strontium ions released cumulatively at each time point was determined by ICP-OES.

2.5. Cell studies

Mouse cell line MC3T3-E1 subclone 4 (ATCC) was used in this study as it is a well known osteoblast model. Cells were cultured at 37° C in 5% CO_2 using culture medium composed of alpha-minimum essential medium (α-MEM, Gibco, Life Technologies) supplemented with 10% (v/v) fetal bovine serum (FBS, Gibco, Life Technologies) and 1% (v/v) antibiotic mixture of penicillin–streptomycin (Sigma), as reported previously.[36] The culture media was changed every 3 days until 80 % confluency. Scaffolds were sterilized with 70 % ethanol for 30 min followed by UV irradiation for 1 h. To wet the scaffolds prior to seeding cells, 0.2 mL complete culture medium was added and centrifuged at 2000 rpm for 2 min to remove trapped air. The culture medium was replaced with 0.2 mL fresh medium containing 2.5 x 10^3 cells and cultured as above.

2.5.1. Assessing cell proliferation

Proliferation of osteoblasts was assessed at 3 and 7 days after seeding using a combination of DNA quantification and nuclear imaging. Cell numbers in the scaffold was quantified by measuring the DNA content in the scaffold using the Picogreen DNA assay.[37] The culture medium was aspirated from the scaffold and replaced with 0.2 mL lysis solution (0.2 mg/ml proteinase K and 0.02 % sodium dodecyl sulfate). After incubation for 24 h at 37°

C, 0.1 ml of the lysate was collected and an equal volume of picogreen reagent solution was added to it following supplier provided procedure. Fluorescence intensity (485 nm excitation and 528 nm emission) of the solution was measured using a microplate reader (Biotek). A standard curve was generated from serial dilutions of a solution of known DNA content. Control scaffolds without cells served as controls.

For nuclear staining, cells in the scaffold were fixed with 3.7% formaldehyde solution in PBS for 30 min and the membrane was permeabilized with 0.2% TritonX-100 for 10 min. Scaffolds were rinsed with PBS and the nucleus was stained with 1 μm/L Sytox green (Invitrogen) for 1 h at 37°C.[38] The stained cells were imaged using an inverted epi-fluorescence microscope (Olympus IX 53).

2.5.3. Differentiation studies

To study the effect of the hybrid nanoparticles in the porous scaffolds on osteogenic differentiation, cells were cultured in complete culture medium containing osteogenic supplements (50 μg/ml ascorbic acid and 10 mM β-glycerophosphate) and the mineralization was assessed at 14 and 21 days. Cells in the scaffolds were fixed with 3.7% formaldehyde solution. Alizarin red-S (ARS) dye was used to stain the mineral deposits on the scaffolds. For mineral quantification, ARS stain was dissolved in 0.5 ml of 5% SDS in 0.5 N HCl for 30 min at room temperature.[39] The absorbance of the solubilised stain was measured at 405 nm using a spectrophotometer. EDX spectroscopy in SEM was used to confirm the chemical nature of the mineral deposits. X-ray micro-computed tomography (Xradia Versa XRM 500) was used to visualize the distribution of the mineral deposits in the scaffolds. The X-ray voltage was set to 80 kV and isotropic resolution was 3 μm. The distance between sample and the detector was maintained at 25 mm. 1600 projections were obtained for each tomogram. Avizo 3D software was used to generate the 3D tomograms and to quantify the

mineral deposits on the scaffold. The threshold for mineral deposits was determined from the intensity histogram of the control scaffolds (without minerals) to eliminate the intensity from the polymer and the voids so as to quantify the intensity from mineral deposits only.

2.6. Statistical analyses

Statistical significance was analysed using 1-way ANOVA (analysis of variance) with Tukey's test for multiple comparisons. Differences were considered as statistically significant for $p < 0.05$.

3. Results and discussion

3.1. Synthesis of hybrid nanoparticles

Attachment of metallic particles on the surface of GO or RGO is mediated either by ionic or weaker van der Waals forces. It has been reported that the negatively charged surface of GO and RGO helps in stabilizing positively charged metallic species on its surface.[22] Hence, to prepare a strontium-eluting graphene hybrid particle, strontium salt must be reduced to metallic strontium. Hydrazine is a common reducing agent used to reduce GO to RGO and also used to reduce metal salts to pure metal.[40]

Synthesis of RGO_Sr was accomplished as shown in Figure 1. GO was synthesized by oxidation of natural graphite. RGO can be prepared from GO by chemical reduction using hydrazine. Hydrazine helps in reducing oxygen-containing functional groups such as epoxy, carbonyl and carboxylate groups on the GO surface.[41] Chemical synthesis routes are preferable for biomedical applications over other techniques such as chemical vapour deposition used to prepare carbonaceous nanomaterials, which involve potentially toxic metals for synthesis.[42] To prepare synthesis of RGO_Sr, hydrazine hydrate was added to dispersed GO solution with strontium nitrate. Hydrazine hydrate helps in reduction of GO and strontium nitrate (metallic salt) by electrophilic elimination reaction.[43] Addition of metallic salt solution resulted in adsorption of reduced metal on the graphene surface thus forming heavier entities which initiate particle sedimentation.[44] Adsorbed metallic particles on RGO surface may also minimize restacking of the carbon sheets.

3.2. Characterization of the nanoparticles

A number of independent techniques were utilized to fully characterize the hybrid nanoparticles. Figure 2a presents the XRD patterns for GO, RGO and RGO_Sr nanoparticles. It shows a characteristic peak at 10.5° for GO and two broad peaks at 24° and 44° for RGO.

These peaks represent d-spacing of 0.82 nm and 0.34 nm for GO and RGO, respectively.[45] The decrease in d-spacing for RGO was due to the reduction of GO by removal of the attached oxygenated functional groups. The broadness of peak at 24° in RGO is believed to be indicative of poorly stacked ordering of sheets, which is attributed to the increase in disorder during reduction of GO.[46] The broad peak at 44° is reported to arise from turbostatic band of disordered carbon materials.[47] The hybrid RGO_Sr nanoparticles show characteristic peaks for both RGO and metallic strontium. The peaks at 25.4°, 29.4°, 42.2°, 48.2° and 52.5° corresponds to the [1 1 1], [2 0 0], [2 2 0], [3 1 1] and [2 2 2] crystal planes of cubic closed pack structure of strontium (JCPDS 89-4045) whereas weak peaks at 44° can be indexed to RGO. The decrease in the intensity of RGO peak suggest that the restacking of RGO sheets was prevented by strontium metallic particles attached at its surface, resulting in better exfoliated RGO_Sr sheets in contrast to RGO. It has been shown that growing metallic particles on GO or RGO results in disappearance or weakening of stacked graphitic peaks because the presence of the metallic particles prevents restacking.[48, 49] Thus, XRD results confirmed the formation of GO, chemical reduction of GO to RGO and the presence of crystalline metallic strontium on the well-exfoliated RGO surface.

Raman spectroscopy is an effective tool for characterizing graphene derived materials. It provides useful information on the nature of order and disorder in the crystalline nature of graphene. Figure 2b presents Raman spectrum for GO, RGO and RGO_Sr nanoparticles. All of the three spectra showed two characteristic peaks corresponding to D and G bands of graphene.[50] The D band is attributed to defective and disordered A_{1g} carbon, whereas G band represents E_{2g} mode of ordered sp^2 carbon atom.[51] The G and D band of GO shifted from 1603 cm^{-1} and 1350 cm^{-1} to 1590 $cm^{-1}$and 1335 cm^{-1}, respectively, in RGO suggeting the reduction of GO to RGO.[52, 53] The I_D/I_G ratio for GO was 1.08 and it increased to 1.45 for RGO. The increase in I_D/I_G ratio correlates with level of disorder and the presence

of defects in graphene.[48] Thus, the increase in I_D/I_G ratio for RGO indicates presence of disordered structure, which corroborates the results from XRD (Figure 2a). The defect sites in the disorderd structure of RGO can serve as an active site for the formation of metallic Sr nanoparticles.[54] Furthermore, RGO_Sr showed I_D/I_G ratio of 1.2, which is higher than that for GO but lower than for RGO. The decrease in I_D/I_G was likely due to the effective stabilization of Sr on defect sites of RGO thereby resulting in a decrease in the D band intensity. Thus, XRD and Raman studies confirmed the reduction of GO to RGO and attachment of metallic strontium on RGO_Sr sheets.

TGA was performed to determine the weight fraction of Sr on the RGO sheet in RGO_Sr. Figure 2c presents the TGA plots for RGO and RGO_Sr. The large initial weight loss (~7 %) for RGO_Sr up to 100° C can be attributed to the removal of physically adsorbed water molecules from hydrophilic metallic (strontium) surface of RGO_Sr. In contrast, RGO showed lower (~2 %) weight loss up to 100° C likely due to the fewer adsorbed water molecules on the hydrophobic RGO surface. This result suggests that the surface decoration of RGO with metallic strontium increased the hydrophilic nature of RGO. At 900° C, the residual mass of RGO_Sr and RGO was 38 % and 16 %, respectively. Therefore, the weight fraction of strontium in RGO_Sr was calculated to be 22 %.

Figure 2d shows XPS spectra of RGO_Sr nanoparticles. The XPS pattern of synthesized RGO_Sr shows a characteristic peak of strontium at 134.3 eV, which matches with the reported XPS peak for crystalline strontium metal.[55] On the other hand, absence of N 1s peak at 405 eV suggest chemical reduction of strontium nitrate by hydrazine hydrate and further stabilization of metallic strontium by RGO on its surface. Thus, XPS also confirmed the presence of strontium metallic particles on RGO surface.

Figure 2e shows a representative TEM image of strontium particles uniformly attached on the surface of RGO sheet in RGO_Sr. Note that strontium particles were seen only on the RGO sheets with no free strontium particles outside the RGO sheets. The crystalline nature of strontium particles on RGO was confirmed by electron diffraction pattern. Uniform growth of strontium particles with average length of 200-300 nm having polydispersity index of 1.22 (Figure S1) on RGO surface confirms the reduction of both strontium salt and GO by hydrazine. Dispersed metallic nanoparticles on graphene sheets help in preventing restacking or aggregation of sheets.[23, 56] As a result, well exfoliated RGO sheets with uniformly decorated strontium particles were obtained as also indicated by XRD result (Figure 2a). Presence of strontium particles only on RGO and not outside RGO sheets further confirms effective stabilization imparted by strontium on RGO surface. To further confirm the attachment of strontium on RGO surface in the hybrid nanoparticles, dispersed RGO_Sr sheets were characterized by SEM. Figure 2f shows the SEM micrograph of RGO_Sr sheets. The EDX spectrum of RGO_Sr sheet revealed the presence of C, O and Sr elemental peaks confirming the existence Sr particles on the surface of RGO sheets. SEM micrographs presented in Figure S2 elucidate the critical role of RGO sheets, which minimize the agglomeration of strontium metallic particles on its surface. Strontium nanoparticles with an average length of 200 nm were uniformly anchored on the RGO surface in the hybrid particles. In contrast, strontium metallic nanoparticles prepared by hydrazine reduction under the same experimental conditions in the absence of graphene tend to aggregate and forms large particles. These results highlight the beneficial role of graphene sheets with large surface area in efficiently supporting uniform growth and good dispersion of fine strontium metallic particles.

Figure 2g presents AFM image RGO_Sr sheets. AFM image confirms RGO surface decorated with strontium metallic particles. The cross-section view along the solid line

indicates an average thickness of about 60 nm for RGO_Sr sheets. The thickness of 60 nm for RGO_Sr sheets suggests that the metallic strontium particles were successfully decorated on both sides of RGO sheets. Strontium nanoparticles were attached on all edges and basal planes of RGO sheets, not merely on the outside RGO sheets corroborating the observations from the TEM (Figure 2e). The lateral dimensions of the RGO sheets were typically ≈ 5 μm. Thus, the size ratio was approximately 1:20 for Sr:RGO in the hybrid nanoparticles.

Figure 2h shows static water contact angle of RGO and RGO_Sr flakes. The water contact angle of RGO flake was 84 ± 5° whereas it decreased to 35 ± 4° for RGO_Sr flake. The decrease in contact angle for RGO_Sr indicates that the presence of metallic Sr particles on RGO surface reduces hydrophobicity in the hybrid nanoparticles. TGA result also indicated the moisture content of the RGO_Sr flakes (Figure 2c) likely due to increased water wettability. Taken together, results from these different techniques established the formation of RGO_Sr hybrid nanoparticles wherein strontium nanocrystals were decorated on the RGO surface.

3.3. Scaffold characterization

A number of different methods are available to prepare macroporous scaffolds for facilitating transport for cell growth and vascularisation for tissue regeneration. The use of a sacrificial porogen is the most widely employed strategy underlying many of these techniques. In this work, we prepared macroporous scaffolds using ammonium bicarbonate as the porogen, as shown schematically in Figure 3a. During immersion in water, in addition to the dissolution of the salt, gas bubbles are also generated from the reaction of ammonium bicarbonate and water. This combination of salt leaching and generation of bubbles yields a polymer scaffold with well distributed and interconnected pores. Representative SEM micrographs of the scaffolds shown in Figure 3b reveal the porous foam architecture of the

scaffolds. Morphology of PCL/RGO and PCL/RGO_Sr scaffolds was similar to that of neat PCL observed here and reported previously.[37] Porosity of the neat PCL, PCL/RGO_5 and PCL_RGO_Sr_5 scaffolds was calculated to be 89 ± 1 %, 85 ± 2 % and 84 ± 2 %, respectively. The porosity of the gas foamed scaffolds decreased marginally with addition of RGO and RGO_Sr nanoparticles. During preparation of the scaffolds, the presence of the particles increases the viscosity of the polymer solution which likely affects its ingress into the salt bed and reduces the porosity marginally. However, the composite scaffolds also showed the macroporous structures seen in neat PCL scaffolds. Scaffolds with higher content of filler could not be prepared as the polymer solution became excessively viscous yielding scaffolds with a non-porous scale at the top. Hence, we were limited to 5% RGO_Sr. Also, excessive filler content may be undesirable as it may impart brittleness to the polymer leading to the problems typically associated with the use of ceramic scaffolds.

Presence of the metallic strontium nanoparticles in the PCL/RGO_Sr scaffolds is shown by arrows in the higher magnification images (Figure 3c inset). The presence of strontium in the scaffolds containing the hybrid nanoparticles was chemically confirmed by EDS (Figure 3c). The Sr peak in the EDS spectra significantly increased with increasing content of the hybrid nanoparticles in the scaffold. To measure changes in wettability of the surface, water contact angle on cast films were measured. Whereas PCL showed contact angle of 73 ± 2°, PCL/RGO_5 and PCL/RGO_Sr_5 show values of 85 ± 1° and 65 ± 1°, respectively. Thus, the use of hydrophilic hybrid nanoparticles increased the water wettability of the polymer.

3.4. Strontium ion release and scaffold degradation

Since strontium ions are known to play an important role in osteogenesis, we measured the release of strontium ions from the PCL/RGO_Sr scaffolds. The concentration

of strontium ions released monotonically increased with increasing content of the hybrid RGO_Sr nanoparticles in the PCL scaffold. The concentration of strontium ion measured after 1 day for PCL/RGO_Sr_1, PCL/RGO_Sr_3 and PCL/RGO_Sr_5 scaffolds was found to be 0.33 ppm, 4.35 ppm, and 15.11 ppm, respectively. Assuming that the mass of strontium eluted from the scaffolds in the culture medium is similar, the concentration in the cell culture is expected to be approximately 0.1 mM, 1.0 mM, and 3.5 mM, respectively.

We further characterized the release kinetics of ions eluted from the scaffolds. The temporal release profiles of strontium ions from PCL/RGO_Sr_5 scaffolds are shown in Figure S3. The plot representing cumulative release for a given time (without change of water) is shown in red. To better mimic the conditions of in vitro cell culture we also measured ion release from scaffolds subject to change of water every 3 days (blue plot). At day 3, strontium ion concentration in aqueous solution was found to be 19 ppm. With change of water, the release of strontium ions decreased from 19 ppm at day 3 to 5 ppm at day 9. However, after day 9, scaffolds eluted ions such that the soluble ion concentration was nearly constant of up to 15 days with marginal decrease over time. The plot of cumulative release (with no change in water) indicates a rapid initial release of strontium ions reaching 40 ppm at day 10 and 48 ppm at day 15. These results suggest that PCL/RGO_Sr_5 scaffolds show an initial burst release of strontium ions putatively from the hybrid nanparticles in close vicinity of the scaffold surface. Thereafter, the continuous release of strontium ions results from well distributed RGO_Sr hybrid particles embedded within the PCL matrix. The sustained release of ions can be envisaged to effectively stimulate cells over sustained periods to augment osteogenesis for bone tissue engineering.

The addition of nanoparticles can significantly affect the degradation of the polymer matrix and thereby the bioresorption of PCL scaffolds in vivo. Figure S4 presents weight loss of PCL, PCL/RGO_5 and PCL/RGO_Sr_5 films due to hydrolytic degradation. PCL and

PCL/RGO_5 films showed slow degradation with 1 wt% mass loss at day 10. In contrast, PCL/RGO_Sr_5 films showed 5 wt% mass loss at day 10. The effect of the hybrid nanoparticles on increased degradation of the polymer scaffold was observed qualitatively up to 10 days by SEM imaging (Figure S5). PCL/RGO_Sr_5 scaffolds at day 0 with smooth pore walls were found to rapidly degrade to yield scaffold walls with micropores as indicated by arrows. Further degradation generated larger micropores possibly arising from merger of smaller micropores. The slow hydrolytic degradation of neat PCL and PCL/RGO_5 composite may be attributed to hydrophobic nature of the films, whereas hydrophilic PCL/RGO_Sr_5 showed faster degradation due to presence of hybrid nanoparticles, as determined by contact angle goniometry reported above. In addition, the dissolution of metallic nanoparticles due to the release of strontium ions facilitates formation of micropores on the scaffold walls.

3.5. Biological studies

Biological response of osteoblasts was studied in the porous scaffolds containing 1%, 3% and 5% hybrid RGO_Sr nanoparticles and compared with RGO-containing and neat PCL scaffolds. Figure 4a presents DNA content on the scaffolds at 3 days and 7 days after cell seeding. The total DNA content of cells in all the scaffolds increased from 3 days to 7 days. There was no statistical difference in DNA content at either 3 days or 7 days between neat PCL and any of the three PCL/RGO scaffolds. However, statistically higher amounts of DNA were observed in all three PCL/RGO_Sr scaffolds compared to neat PCL at both 3 days and 7 days. At day 7, although the mean DNA content increased with increase in RGO_Sr content, these differences were not statistically significant. However, at day 7, PCL/RGO_Sr_5 scaffold showed significantly higher cell proliferation than that in neat PCL, PCL/RGO_1 and PCL/RGO_3. Control scaffolds of PCL, PCL/RGO and PCL/RGO_Sr revealed a negligible amount of DNA content (< 1 ng) in the absence of cells confirming that the DNA

measured in the scaffolds by this assay in Figure 4a is a measure of cell number. Figure 4b compiles representative fluorescence micrographs of stained cellular nuclei in the scaffolds at 3 days and 7 days further confirming the presence of cells in the scaffolds. Taken together, results of the DNA assay and the fluorescence imaging suggest that all the scaffolds supported cell proliferation. Although the addition of RGO to PCL did not inhibit the proliferation of osteoblasts, it was unable to stimulate cell proliferation. The addition of hybrid nanoparticles to PCL, however, enhanced osteoblast proliferation in the scaffolds than that seen in neat PCL or the RGO composites, owing to hydrophilic nature of hybrid nanoparticles. It has been reported that hydrophilic surfaces promote favourable protein adsorption to augment better cell adhesion and proliferation.[57] Some studies have also reported that strontium ion help in increased cell replication of osteoblasts,[58] underscoring the need for such hybrid nanoparticles for bone tissue engineering.

Deposition of calcium phosphate in the extracellular matrix is indicative of osteogenesis and is taken as a marker for bone regeneration. The bioactivity of a scaffold for bone tissue engineering is widely assessed by examining the *in vitro* mineralization by osteoblasts cultured in the scaffold.[59, 60] Figure 5a presents a quantitative comparison of mineral deposits in the different scaffolds. At day 14, mineral deposits were seen in all the scaffolds. Furthermore, the mineral content in all the scaffolds increased by day 21. PCL and PCL/RGO scaffolds did not show any significant difference in mineral content at either day 14 or day 21. On the other hand, the PCL/RGO_Sr scaffolds showed higher mineral content compared to neat PCL and the PCL/RGO scaffolds. These differences were more pronounced and statistically significant as the content of the hybrid RGO_Sr particles increased. PCL/RGO_Sr_5 scaffold showed the highest mineral deposition among all the scaffolds evaluated at both 14 days and 21 days. Note that the mineral content in the PCL/RGO_Sr_5 was more than 50 % higher than that in neat PCL scaffolds at 21 days. Figure 5b shows the

EDX spectra of the mineralized scaffolds in osteogenic supplements confirming the presence of calcium phosphate in the scaffold.

X-ray micro-computed tomography is a useful technique to characterize 3D architecture of scaffolds, and to examine bone tissue repair and changes in the scaffold after mineralization on implantation.[61] Higher density calcium deposits appear as brighter regions in contrast to the lower density material such as the polymer scaffold. Figure 6 shows representative 3D reconstructions of the neat PCL, PCL/RGO_5 and PCL/RGO_Sr_5 scaffolds after mineralization at 21 days and the as-synthesized PCL/RGO_Sr_5 scaffold. The tomograms reveal an interconnected porous architecture of the scaffold in 3D. Presence of mineral deposits at 21 days is indicated by the presence of increased bright regions in the tomograms, which appear to be nearly uniformly distributed within the scaffold. Results of mineral quantification showed presence of 1.3%, 1.1 % and 4.6% mineral content in the PCL, PCL/RGO_5 and PCL/RGO_Sr_5 scaffolds, respectively. Note that the strontium nanoparticles in the scaffolds containing the hybrid particles are smaller than the resolution of the image and the content is sufficiently low such that the particles cannot be clearly discerned. Thus, results of X-ray tomography indicating osteogenesis leading to mineralization corroborate the findings from staining and EDX analysis of the mineralized scaffolds.

We further assessed if the hybrid nanoparticles were sufficient to induce osteogenesis leading to mineralization in growth medium even in the absence of osteoinductive factors. Figure S6 presents quantitative comparison of mineral deposits in PCL, PCL/RGO_5 and PCL/RGO_Sr_5 scaffolds at days 14 and 21. Although the mineral content was lower than the in scaffold cultured with osteogenic media, the trend in mineralization pattern was similar. PCL/RGO_Sr_5 showed the highest mineral content which was nearly double the mineral content in neat PCL and PCL/RGO_5 scaffolds at both 14 and 21 days. Thus, the

strontium ions were sufficient to induce osteogenesis even in the absence of soluble osteo-indutive factors. Figure S6 also demonstrates that an insignificant amount of ARS stain was observed in control scaffolds without cells thereby confirming that measured absorbance resulted from minerals deposited by the osteoblasts in the scaffolds.

Thus, the findings of this study demonstrate that the RGO_Sr hybrid nanoparticles significantly augmented bone tissue formation in the scaffolds in contrast to the use of RGO nanoparticles. We attribute this to the release of strontium ions in the culture medium from the scaffolds containing the hybrid nanoparticles.[62] It has been shown metallic strontium promotes cell proliferation and differentiation of pre-osteoblasts resulting in enhanced mineralization and osteogenesis.[63, 64] Furthermore, other studies have also confirmed that strontium as a divalent cation helps in activation of calcium sensing receptors and osteoblast markers.[65, 66] It has been observed that 3 mM of strontium ions markedly enhanced osteoblast activity.[62, 67] This is comparable to the concentration of strontium ions eluted by the hybrid scaffolds, as reported above. Moreover, the local concentration at the cell-scaffold interface is likely to be higher and thus, more effective at influencing cell function than what can be predicted from measurements of bulk strontium concentration.

Graphene is a novel nanomaterial and its potential for biomedical applications is being studied only in recent years. Understanding the toxicity and genotoxicity associated with graphene is an active area of research. Most of these studies have been reported for particles in the form of colloidal dispersion added to the medium to cells cultured in vitro. The toxicity of graphene depends on the concentration, particle size, functionalization, exposure time, etc.[68, 69] Many of these studies have suggested that a high concentration of graphene induces toxicity. A few studies have observed genotoxicity at lower concentration.[70] There are fewer studies on the use of graphene to prepare scaffolds for tissue engineering. These have typically involved assessing the cell response in vitro and have

reported improved cell response. The duration of these in vitro studies is insufficient for the full degradation of the polymer scaffolds and the release of all the nanoparticles. The long term effects and associated risks, if any, of using graphene in tissue scaffolds in vivo is not well understood and will require a more thorough assessment prior to clinical use. Nevertheless, it has been reported that RGO can be added to PCL matrix to improve the mechanical property.[71] However, RGO lacks functional or biochemical groups that may stimulate osteogenesis. Strontium containing biomaterials are being increasingly developed for orthopaedic applications. The release of strontium form the biomaterial surface in physiological environment is believed to promote cell proliferation, differentiation and enhanced the metabolic activity of osteoblasts.[14, 15, 72] The objective of this work was to demonstrate the utility of developing hybrid nanoparticles for tissue engineering and the advantages it may offer. The findings presented here demonstrate that hybrid RGO_Sr nanoparticles can help in dispersion of fine metallic nanoparticles. Hybrid nanoparticles that elute strontium ions in physiological solutions can be successfully utilized to prepare multifunctional composites with good mechanical and osteoinductive properties. These polymer composites incorporating hybrid nanoparticles are likely to find use in the next generation of biomaterials for tissue engineering.

4. Conclusion

Facile synthesis of hybrid particles composed of graphene sheets decorated with metallic strontium nanoparticles was demonstrated. The physical dimensions, chemical composition and crystallographic nature of these hybrid particles were extensively characterized using different techniques. 3D tissue scaffolds were prepared using these hybrid particles in polymer matrix, which were found to elute significant concentration of strontium ions in aqueous environment. Osteoblast proliferation and differentiation significantly increased in scaffolds containing the RGO_Sr particles. Thus, the use of multifunctional hybrid nanoparticles offers a promising route to prepare the next-generation scaffolds for regenerative medicine.

Acknowledgements

This work was funded by the Science and Engineering Research Board of the Department of Science and Technology (DST-SERB), India. K.C. gratefully acknowledges the Ramanujan fellowship from DST.

References

1. X. Sun, Z. Liu, K. Welsher, J.T. Robinson, A. Goodwin, S. Zaric and H. Dai, *Nano Research*, 2008, **1**, 203-212.
2. Y. Liu, D. Yu, C. Zeng, Z. Miao and L. Dai, *Langmuir*, 2010, **26**, 6158-6160.
3. W.C. Lee, C.H.Y. Lim, H. Shi, L.A. Tang, Y. Wang, C.T. Lim and K.P. Loh, *Acs Nano*, 2011, **5**, 7334-7341.
4. L. Yang, L. Zhang and T.J. Webster, *Nanomedicine*, 2011, **6**, 1231-1244.
5. N. Li, X. Zhang, Q. Song, R. Su, Q. Zhang, T. Kong, L. Liu, G. Jin, M. Tang and G. Cheng, *Biomaterials*, 2011, **32**, 9374-9382.
6. D. Depan, B. Girase, J. Shah and R. Misra, *Acta Biomaterialia*, 2011, **7**, 3432-3445.
7. Q. Hu, Z. Tan, Y. Liu, J. Tao, Y. Cai, M. Zhang, H. Pan, X. Xu and R. Tang, *Journal of Materials Chemistry*, 2007, **17**, 4690-4698.
8. J.L. Moreau and H.H. Xu, *Biomaterials*, 2009, **30**, 2675-2682.
9. G.-Y. Jung, Y.-J. Park and J.-S. Han, *Journal of Materials Science: Materials in Medicine*, 2010, **21**, 1649-1654.
10. P.J. Marie, *Current Opinion in Rheumatology*, 2006, **18**, S11-S15.
11. K. Qiu, X.J. Zhao, C.X. Wan, C.S. Zhao and Y.W. Chen, *Biomaterials*, 2006, **27**, 1277-1286.
12. J. Reginster, *Current Pharmaceutical Design*, 2002, **8**, 1907-1916.
13. J.-Y. Reginster, E. Seeman, M. De Vernejoul, S. Adami, J. Compston, C. Phenekos, J.-P. Devogelaer, M.D. Curiel, A. Sawicki and S. Goemaere, *The Journal of Clinical Endocrinology & Metabolism*, 2005, **90**, 2816-2822.
14. J. Isaac, J. Nohra, J. Lao, E. Jallot, J.-M. Nedelec, A. Berdal and J.-M. Sautier, *Eur Cell Mater*, 2011, **21**, 130-143.
15. E. Boanini, P. Torricelli, M. Fini and A. Bigi, *Journal of Materials Science: Materials in Medicine*, 2011, **22**, 2079-2088.
16. M. O'Donnell, P. Candarlioglu, C. Miller, E. Gentleman and M. Stevens, *Journal of Materials Chemistry*, 2010, **20**, 8934-8941.
17. M. Erol, A. Özyuğuran, Ö. Özarpat and S. Küçükbayrak, *Journal of the European Ceramic Society*, 2012, **32**, 2747-2755.
18. R.J. White, R. Luque, V.L. Budarin, J.H. Clark and D.J. Macquarrie, *Chemical Society Reviews*, 2009, **38**, 481-494.

19. A.R. Boccaccini, M. Erol, W.J. Stark, D. Mohn, Z. Hong and J.F. Mano, *Composites Science and Technology*, 2010, **70**, 1764-1776.
20. P. Dallas, V.K. Sharma and R. Zboril, *Advances in Colloid and Interface Science*, 2011, **166**, 119-135.
21. X. Zhou, X. Huang, X. Qi, S. Wu, C. Xue, F.Y. Boey, Q. Yan, P. Chen and H. Zhang, *The Journal of Physical Chemistry C*, 2009, **113**, 10842-10846.
22. G. Goncalves, P.A. Marques, C.M. Granadeiro, H.I. Nogueira, M. Singh and J. Gracio, *Chemistry of Materials*, 2009, **21**, 4796-4802.
23. Y. Zou and Y. Wang, *Nanoscale*, 2011, **3**, 2615-2620.
24. T. Yu, J. Lin, J. Xu, T. Chen, S. Lin and X. Tian, *Composites Science and Technology*, 2007, **67**, 3219-3225.
25. C. Tang, L. Xiang, J. Su, K. Wang, C. Yang, Q. Zhang and Q. Fu, *The Journal of Physical Chemistry B*, 2008, **112**, 3876-3881.
26. Y. Xue, H. Chen, D. Yu, S. Wang, M. Yardeni, Q. Dai, M. Guo, Y. Liu, F. Lu and J. Qu, *Chemical Communications*, 2011, **47**, 11689-11691.
27. T. Lu, L. Pan, H. Li, G. Zhu, T. Lv, X. Liu, Z. Sun, T. Chen and D.H. Chua, *Journal of Alloys and Compounds*, 2011, **509**, 5488-5492.
28. A.N. Sidorov, G.W. Sławiński, A. Jayatissa, F.P. Zamborini and G.U. Sumanasekera, *Carbon*, 2012, **50**, 699-705.
29. C. Shan, H. Yang, D. Han, Q. Zhang, A. Ivaska and L. Niu, *Biosensors and Bioelectronics*, 2010, **25**, 1070-1074.
30. M.R. Das, R.K. Sarma, R. Saikia, V.S. Kale, M.V. Shelke and P. Sengupta, *Colloids and Surfaces B: Biointerfaces*, 2011, **83**, 16-22.
31. L. Liu, J. Liu, Y. Wang, X. Yan and D.D. Sun, *New Journal of Chemistry*, 2011, **35**, 1418-1423.
32. W.S. Hummers Jr and R.E. Offeman, *Journal of the American Chemical Society*, 1958, **80**, 1339-1339.
33. K. Chatterjee, A.M. Kraigsley, D. Bolikal, J. Kohn and C.G. Simon, *Journal of Functional Biomaterials*, 2012, **3**, 173-182.
34. R. Zhang and P.X. Ma, *Journal of Biomedical Materials Research*, 1999, **44**, 446-455.
35. S. Kumar, A. Mishra and K. Chatterjee, *Materials Research Express*, 2014, **1**, 045302.
36. S. Kumar, S. Bose and K. Chatterjee, *RSC Advances*, 2014, **4**, 19086-19098.

37. G. Kumar, C.K. Tison, K. Chatterjee, P.S. Pine, J.H. McDaniel, M.L. Salit, M.F. Young and C.G. Simon Jr, *Biomaterials*, 2011, **32**, 9188-9196.
38. K. Chatterjee, L. Sun, L.C. Chow, M.F. Young and C.G. Simon Jr, *Biomaterials*, 2011, **32**, 1361-1369.
39. Y. Bi, C.H. Stuelten, T. Kilts, S. Wadhwa, R.V. Iozzo, P.G. Robey, X.-D. Chen and M.F. Young, *Journal of Biological Chemistry*, 2005, **280**, 30481-30489.
40. S. Stankovich, D.A. Dikin, R.D. Piner, K.A. Kohlhaas, A. Kleinhammes, Y. Jia, Y. Wu, S.T. Nguyen and R.S. Ruoff, *Carbon*, 2007, **45**, 1558-1565.
41. P.-G. Ren, D.-X. Yan, X. Ji, T. Chen and Z.-M. Li, *Nanotechnology*, 2011, **22**, 055705-055712.
42. C. Ge, Y. Li, J.-J. Yin, Y. Liu, L. Wang, Y. Zhao and C. Chen, *NPG Asia Materials*, 2012, **4**, e32.
43. M.K. Singh, E. Titus, R. Krishna, R. Hawaldar, G. Goncalves, P. Marques and J. Gracio, *Journal of Nanoscience and Nanotechnology*, 2012, **12**, 6731-6736.
44. C. Xu, X. Wang and J. Zhu, *The Journal of Physical Chemistry C*, 2008, **112**, 19841-19845.
45. A.B. Bourlinos, D. Gournis, D. Petridis, T. Szabó, A. Szeri and I. Dékány, *Langmuir*, 2003, **19**, 6050-6055.
46. Y. Zhu, M.D. Stoller, W. Cai, A. Velamakanni, R.D. Piner, D. Chen and R.S. Ruoff, *Acs Nano*, 2010, **4**, 1227-1233.
47. B.Y.S. Chang, N.M. Huang, M.N. An'amt, A.R. Marlinda, Y. Norazriena, M.R. Muhamad, I. Harrison, H.N. Lim and C.H. Chia, *International Journal of Nanomedicine*, 2012, **7**, 3379.
48. J. Shen, M. Shi, N. Li, B. Yan, H. Ma, Y. Hu and M. Ye, *Nano Research*, 2010, **3**, 339-349.
49. C. Xu, X. Wang, J. Zhu, X. Yang and L. Lu, *Journal of Materials Chemistry*, 2008, **18**, 5625-5629.
50. R. Nemanich and S. Solin, *Physical Review B*, 1979, **20**, 392-401.
51. F. Tuinstra and J.L. Koenig, *The Journal of Chemical Physics*, 1970, **53**, 1126-1130.
52. W. Chen, L. Yan and P. Bangal, *The Journal of Physical Chemistry C*, 2010, **114**, 19885-19890.
53. Z. Ji, X. Shen, G. Zhu, H. Zhou and A. Yuan, *Journal of Materials Chemistry*, 2012, **22**, 3471-3477.

54. D. Pan, S. Wang, B. Zhao, M. Wu, H. Zhang, Y. Wang and Z. Jiao, *Chemistry of Materials*, 2009, **21**, 3136-3142.
55. V. Young and T. Otagawa, *Applications of Surface Science*, 1985, **20**, 228-248.
56. S.Q. Chen and Y. Wang, *Journal of Materials Chemistry*, 2010, **20**, 9735-9739.
57. C.J. Wilson, R.E. Clegg, D.I. Leavesley and M.J. Pearcy, *Tissue Engineering*, 2005, **11**, 1-18.
58. O. Fromigué, E. Haÿ, A. Barbara, C. Petrel, E. Traiffort, M. Ruat and P.J. Marie, *Journal of Cellular and Molecular Medicine*, 2009, **13**, 2189-2199.
59. L.L. Hench and J.M. Polak, *Science*, 2002, **295**, 1014-1017.
60. K. Rezwan, Q. Chen, J. Blaker and A.R. Boccaccini, *Biomaterials*, 2006, **27**, 3413-3431.
61. R. Cancedda, A. Cedola, A. Giuliani, V. Komlev, S. Lagomarsino, M. Mastrogiacomo, F. Peyrin and F. Rustichelli, *Biomaterials*, 2007, **28**, 2505-2524.
62. V. Nardone, S. Fabbri, F. Marini, R. Zonefrati, G. Galli, A. Carossino, A. Tanini and M.L. Brandi, *International Journal of Biomaterials*, 2012, **2012**, 865291.
63. E. Canalis, M. Hott, P. Deloffre, Y. Tsouderos and P. Marie, *Bone*, 1996, **18**, 517-523.
64. A. Barbara, P. Delannoy, B. Denis and P. Marie, *Metabolism*, 2004, **53**, 532-537.
65. L.-L. Zhu, S. Zaidi, Y. Peng, H. Zhou, B.S. Moonga, A. Blesius, I. Dupin-Roger, M. Zaidi and L. Sun, *Biochemical and Biophysical Research Communications*, 2007, **355**, 307-311.
66. Z. Saidak and P.J. Marie, *Pharmacology & therapeutics*, 2012, **136**, 216-226.
67. S. Choudhary, P. Halbout, C. Alander, L. Raisz and C. Pilbeam, *Journal of Bone and Mineral Research*, 2007, **22**, 1002-1010.
68. O. Akhavan, E. Ghaderi and A. Akhavan, *Biomaterials*, 2012, **33**, 8017-8025.
69. Y. Chang, S.-T. Yang, J.-H. Liu, E. Dong, Y. Wang, A. Cao, Y. Liu and H. Wang, *Toxicology Letters*, 2011, **200**, 201-210.
70. L. De Marzi, L. Ottaviano, F. Perrozzi, M. Nardone, S. Santucci, J. De Lapuente, M. Borras, E. Treossi, V. Palermo and A. Poma, *Journal of biological regulators and homeostatic agents*, 2013, **28**, 281-289.
71. J. Zhang and Z. Qiu, *Industrial & Engineering Chemistry Research*, 2011, **50**, 13885-13891.
72. E. Gentleman, Y.C. Fredholm, G. Jell, N. Lotfibakhshaiesh, M.D. O'Donnell, R.G. Hill and M.M. Stevens, *Biomaterials*, 2010, **31**, 3949-3956.

List of Tables:

Table 1: Composition and nomenclature of the different scaffolds

Sample Code	Composition		
	mg of RGO/ g of PCL	mg of RGO_Sr/ g of PCL	mg of Sr/ g of PCL
PCL	0	0	0
PCL/RGO_1	10	0	0
PCL/RGO_3	30	0	0
PCL/RGO_5	50	0	0
PCL/RGO_Sr_1	0	10	2.2
PCL/RGO_Sr_3	0	30	6.6
PCL/RGO_Sr_5	0	50	11.0

Figure captions:

Figure 1: Schematic showing synthesis and use of RGO_Sr in macroporous scaffolds for bone tissue engineering

Figure 2: Characterization of synthesized nanoparticles (a) XRD profiles of GO, RGO and RGO_Sr nanoparticles, (b) Raman spectra of GO, RGO and RGO_Sr nanoparticles, (c) TGA thermograph of RGO and RGO_Sr, (d) XPS spectra for RGO_Sr nanoparticles, (e) TEM micrograph of dispersed RGO_Sr flakes with inset presenting the electron diffraction pattern of RGO_Sr, (f) SEM micrograph with EDX spectrum of RGO_Sr sheets, (g) AFM image and (h) Water contact angle of RGO and RGO_Sr flakes

Figure 3: (a) Schematic illustration of preparation of scaffolds by gas foaming, (b) SEM micrographs of macroporous PCL, PCL/RGO_5 and PCL/RGO_Sr_5 scaffolds and (c) EDX spectrum of PCL/RGO_Sr porous scaffold

Figure 4: (a) DNA quantification of osteoblasts cultured in the porous PCL, PCL/RGO and PCL/RGO_Sr scaffolds. Results represent average ± SD for n = 5. Statistically significant differences ($p < 0.05$) compared to neat PCL and PCL/RGO_1 and PCL/RGO_3 are indicated by the symbols ∗,♦ and •, respectively, and (b) Fluorescent micrographs of cell nuclei in the scaffolds at 3 days, and 7 days (scale bar = 0.1 mm)

Figure 5: (a) Quantification of mineral stained by ARS dye on different scaffolds at 14 days and 21 days. Results represent average ± SD for n = 5. Statistically significant differences ($p < 0.05$) compared to neat PCL and PCL/RGO_1 and PCL/RGO_3, PCL/RGO_5, PCL/RGO_Sr_1 and PCL/RGO_Sr_3 are indicated by the symbols ∗,♦, •, o, ∅ and Φ, respectively, (b) EDX spectra for neat PCL, PCL/RGO_5 and PCL/RGO_Sr_5 mineralised scaffold at 21 days

Figure 6: X-ray micro-computed tomograms of mineralized scaffolds of PCL, PCL/RGO_5, PCL/RGO_Sr_5 at day 21 and as synthesized (non mineralized) PCL/RGO_Sr_5 scaffold

Figure 1

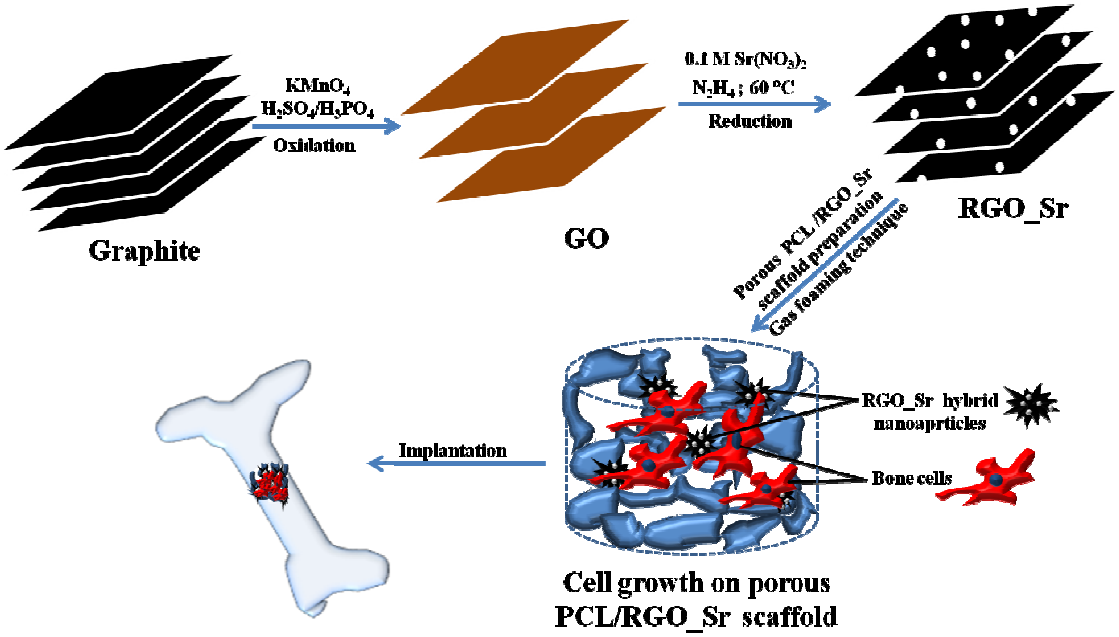

Figure 2

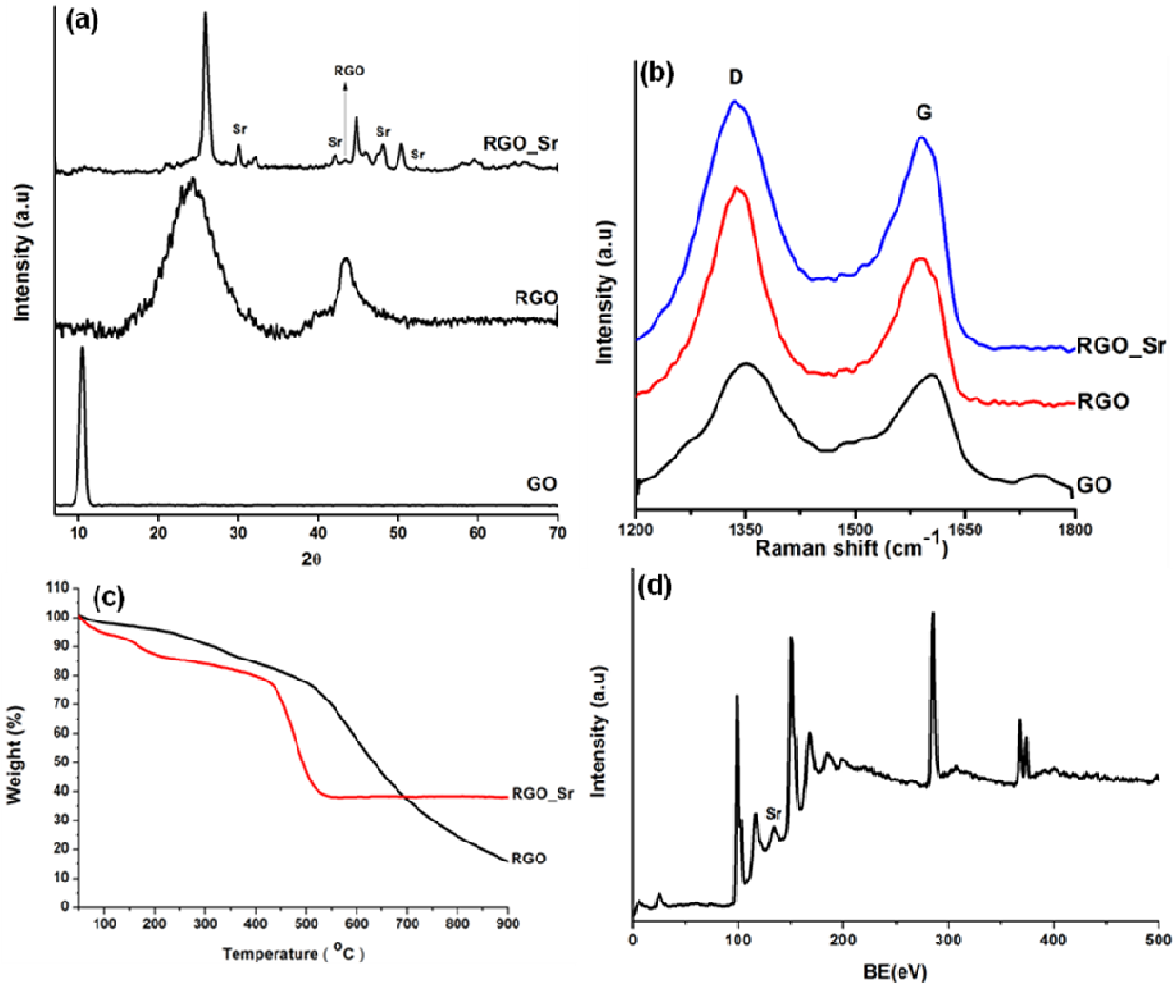

Figure 2 cont.

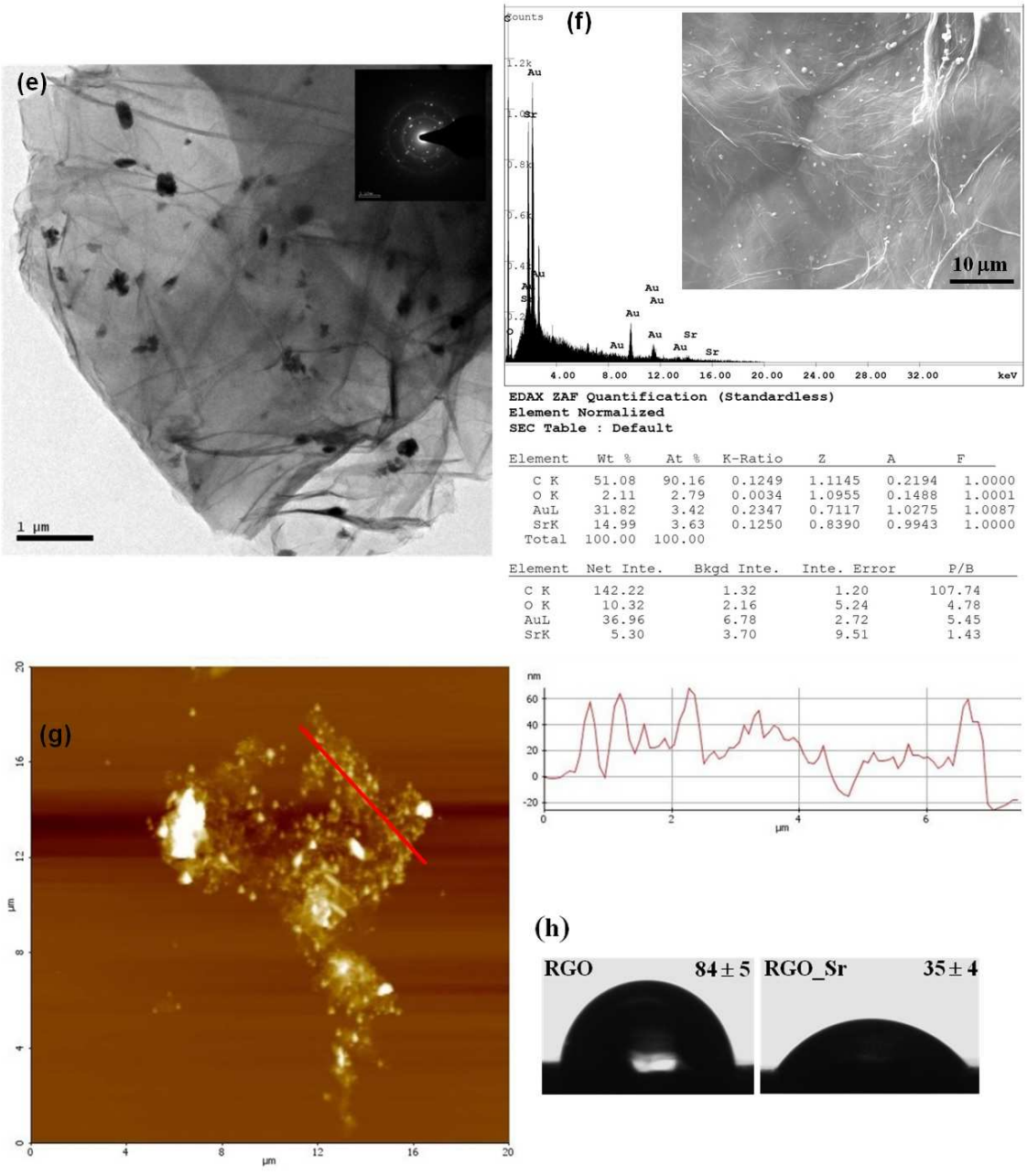

Figure 3

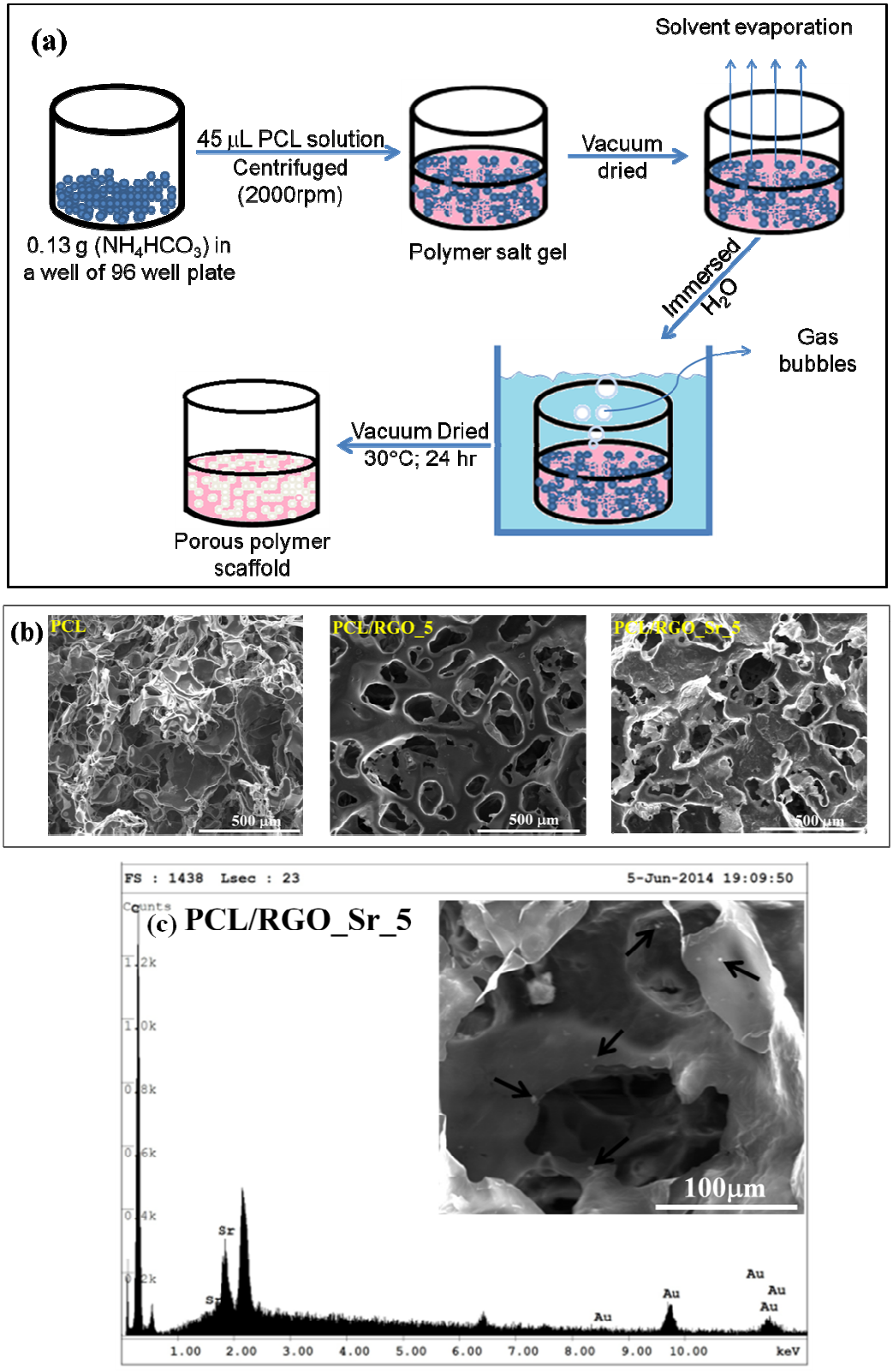

Figure 4

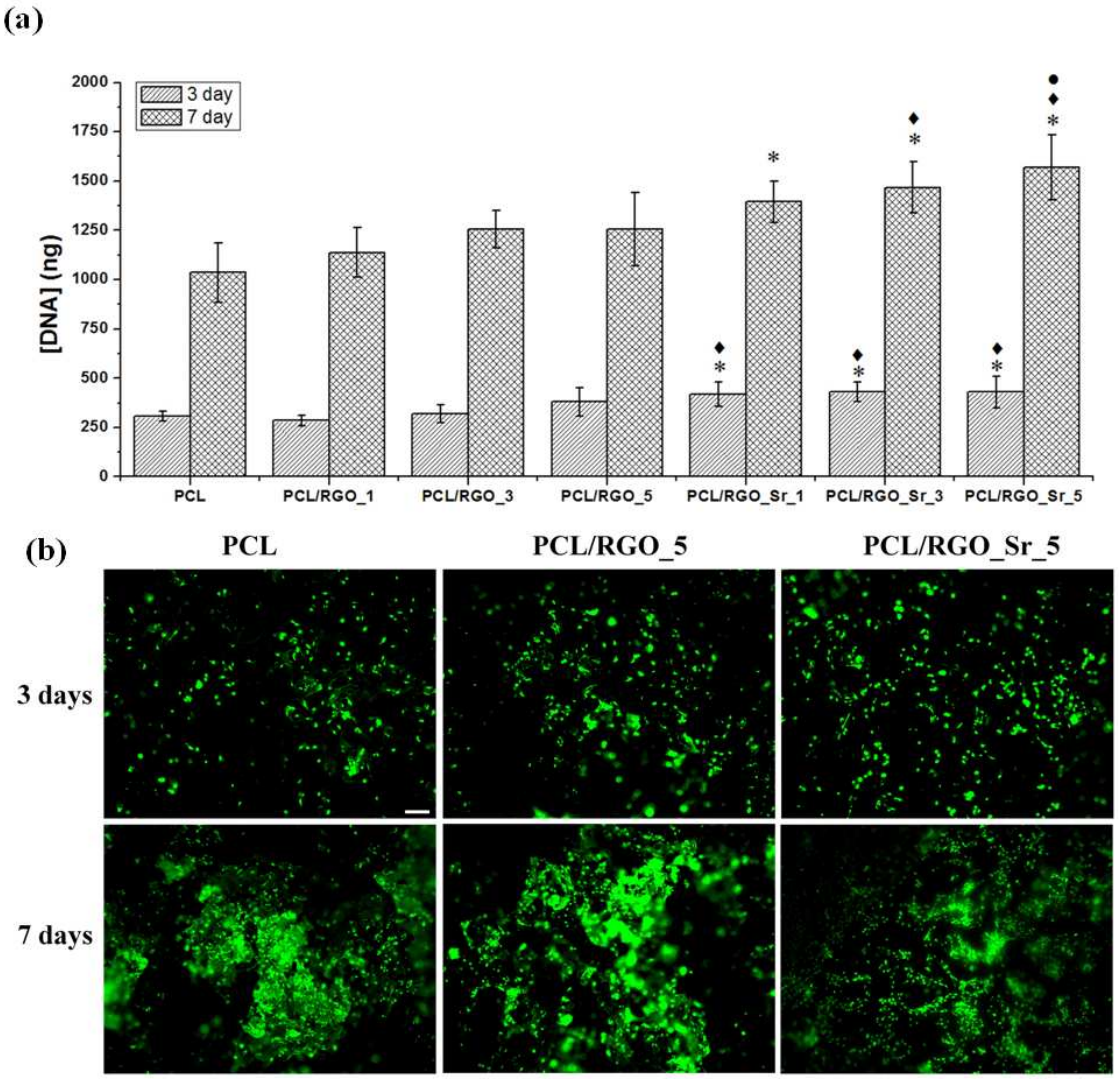

Figure 5

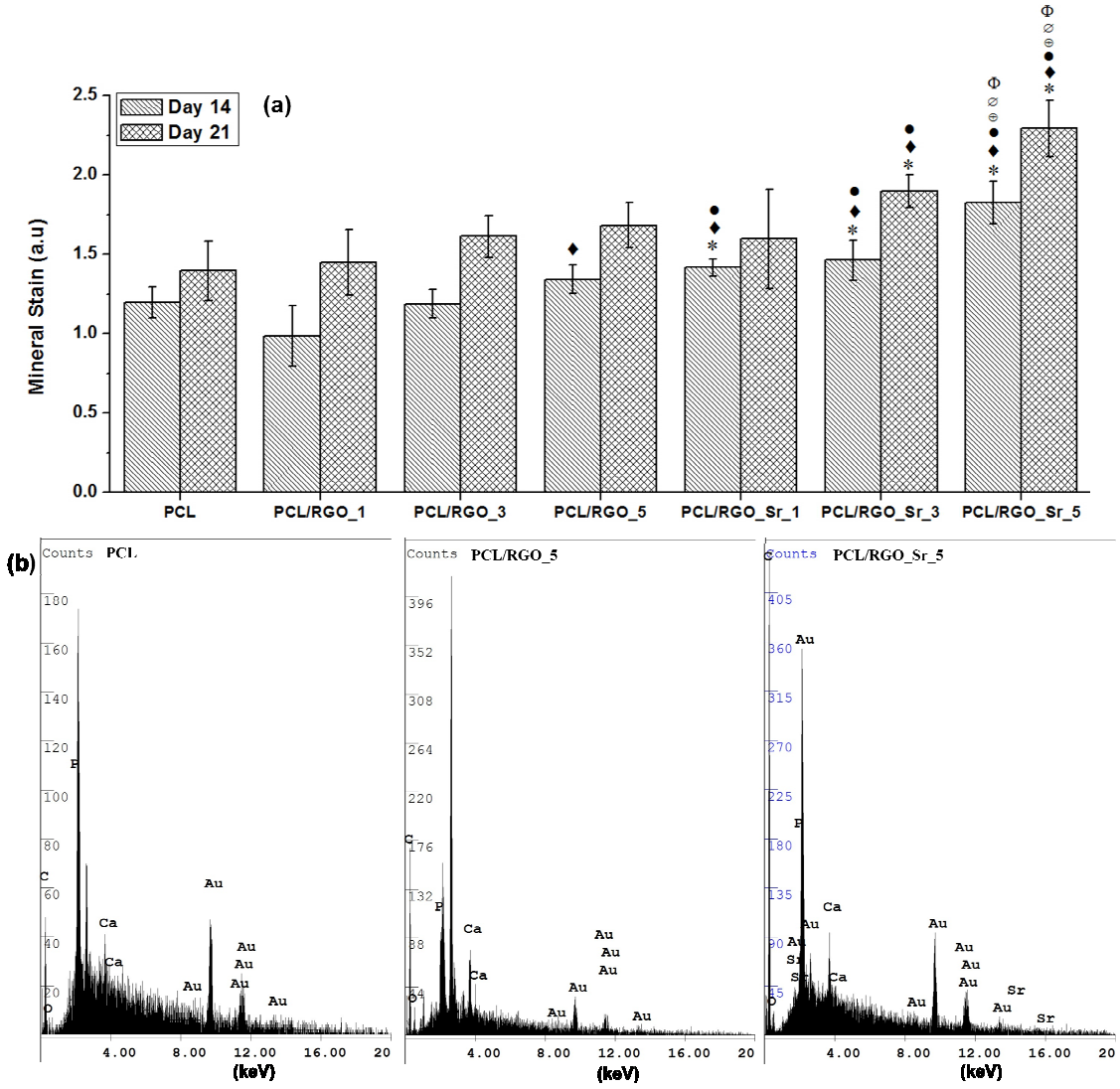

Figure 6